

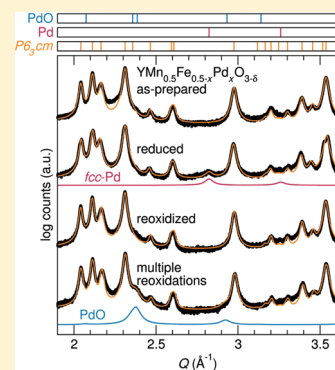
Pd²⁺/Pd⁰ Redox Cycling in Hexagonal YMn_{0.5}Fe_{0.5}O₃: Implications for Catalysis by PGM-Substituted Complex Oxides

Joshua A. Kurzman,[†] Jun Li,[†] Thomas D. Schladt,[†] César R. Parra,[†] Xiaoying Ouyang,[†] Ryan Davis,[†] Jeffrey T. Miller,[‡] Susannah L. Scott,^{*,†} and Ram Seshadri^{*,†}

[†]Department of Chemistry and Biochemistry, Materials Research Laboratory, Department of Chemical Engineering, and Materials Department, University of California, Santa Barbara, California 93106, United States

[‡]Chemical Sciences and Engineering Division, Argonne National Laboratory, Argonne, Illinois 60439, United States

ABSTRACT: Complex oxides—containing at least two different cations on crystallographically distinct sites—have recently been shown to display redox cycling of platinum group metals (PGMs), such as Pd; for example, Pd-substituted complex oxides can reversibly extrude metallic Pd under reducing conditions and then reincorporate Pd²⁺ ions into the lattice under oxidizing conditions. The title compounds, YMn_{0.5}Fe_{0.5-x}Pd_xO_{3-δ} (0 ≤ x ≤ 0.07) crystallizing in the noncentrosymmetric YMnO₃ structure, were prepared using a sol-gel process at 800 °C, and the structures were refined from high-resolution synchrotron X-ray powder diffraction data. Their redox cycling behavior was monitored using synchrotron X-ray diffraction and EXAFS studies. In contrast to the previously studied complex oxide host compounds, YMn_{0.5}Fe_{0.5-x}Pd_xO_{3-δ} is only modestly tolerant to cycling: repeated redox cycling leads to the formation of PdO, which, on the time-scale of the oxidation cycles, does not reincorporate in the complex oxide lattice. Both oxidized and reduced samples were tested for the oxidation of CO to CO₂ under CO-lean conditions. YMn_{0.5}Fe_{0.5-x}Pd_xO_{3-δ} performs essentially as well as previously studied YFe_{1-x}Pd_xO_{3-δ}. The CO oxidation light-off characteristics of the hexagonal hosts are very similar to finely dispersed PdO. Despite evidence that Pd is almost fully dispersed as divalent ions in the host lattice, which is presumably accompanied by the concurrent creation of oxygen vacancies (2 Pd²⁺:1 V_{O2-}), the as-prepared hexagonal materials do not display any significant improvement in catalytic activity as a function of Pd substitution level. This suggests that the corner-connected trigonal bipyramids that characterize this structural family do not enable the transport of oxygen through the bulk of the lattice. The study casts light on factors in the solid-state chemistry of precious metal-substituted complex oxides that influence the efficacy of redox cycling of the precious metal, and catalytic performance.



INTRODUCTION

While the activity of bulk oxides for reactions relevant to automotive exhaust control has been recognized since the 1970s,¹⁻⁴ the finding by Tanaka and co-workers that perovskite LaFe_{0.57}Co_{0.38}Pd_{0.05}O₃ can reversibly extrude and reincorporate palladium in response to redox fluctuations characteristic of an automotive exhaust stream⁵ has greatly piqued the interest of researchers into catalysis by substituted complex oxides. Precious metal-substituted complex oxides are interesting alternatives to more conventional metal nanoparticle-on-oxide catalysts, offering comparable activities with increased lifetimes at significantly reduced metal loadings.⁶ A number of complex oxide systems are known to accommodate the substitution of platinum group metal (PGM) ions,⁷⁻¹² but only a few have been shown to display so-called “intelligent” behavior, whereby PGM ions migrate out of the host, forming metallic nanoparticles under reducing conditions, and re-enter the oxide lattice as fully dispersed ions under oxidizing conditions.^{5,13-18} The concerted egress/ingress behavior has been suggested as the mechanism that suppresses nanoparticle sintering under operating conditions in a catalytic converter.⁵ Sintering of the active phase is a primary mechanism for deactivation in conventional supported

catalysts, and ablation of the sintered PGM particles from the oxide results in metal pollution.

Hegde and co-workers have contributed an extensive body of work addressing the catalytic activity of binary oxide-based compounds substituted with PGM ions.¹⁹ Much of this work has focused on CeO₂ as a host,^{20,21} and concurrent substitution by early transition metals²²⁻²⁴ or main group metals^{25,26} has been shown to be an effective route toward increasing the oxygen storage capacity and activity of ceria-based catalysts, both of which are promoted by the substitution of PGM ions, such as Pd²⁺. While multiple cations are often present in these binary oxide-based materials, the cations are disordered over a single crystallographic site. These are distinct from *complex* oxides, in which two different cations (or more) occupy discrete crystallographic sites. Although it has been suggested that PGM ions can be extruded and reincorporated into the pseudobinary oxide hosts,^{24,25} the low levels of substitution typically explored (ca. 1–2 mol %) are at the detection limits of phase identification by conventional laboratory powder diffraction, particularly given

Received: March 6, 2011

Published: July 29, 2011

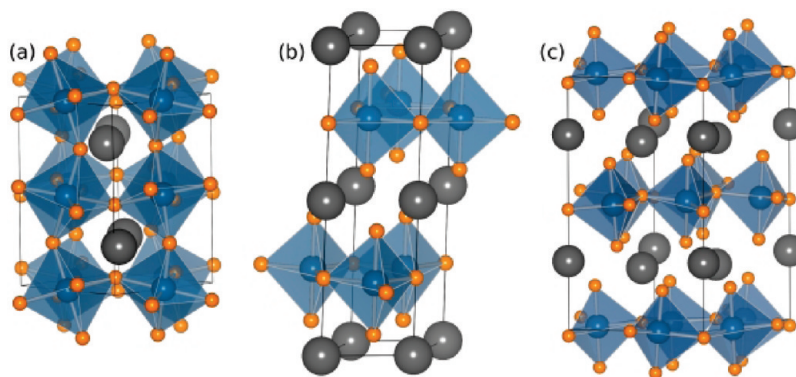


Figure 1. Unit cell depictions of (a) YBO_3 perovskite, space group $Pnma$, (b) the Be_3N_2 hexagonal structure adopted by metastable YFeO_3 , space group $P6_3/mmc$, and (c) the room-temperature YMnO_3 structure, space group $P6_3cm$. B site rendered as coordination polyhedra.

that very fine particles are often produced upon reduction, and it is unclear whether the PGMs re-enter the binary oxide-based hosts or oxidize to small PdO particles. In this regard, a general strategy employed by us is the preparation of more heavily substituted samples and the application of high-resolution synchrotron X-ray or neutron diffraction studies for evaluating the structure and phase composition in crystalline PGM-substituted materials. To this end, our objective has not been the preparation of high surface area materials optimized for catalysis.

Given that the platinum group and noble metals are the most oxophilic transition elements, the selection and development of host lattices requires an understanding of the factors that promote stabilization of PGM ions in oxide environments. Our comparison of two quaternary oxides of Pd^{2+} and Au^{3+} , $\text{La}_2\text{BaPdO}_5$ and $\text{La}_4\text{LiAuO}_8$, revealed that their exceptional thermal stability and resistance to reduction can be attributed to strongly covalent Pd–O and Au–O bonding that is driven by the highly electropositive nature of the La^{3+} , Ba^{2+} , and Li^+ cations.²⁷ Indeed, all of the materials in which PGM substitution has been reported contain electropositive counterions. For example, even the prototypical perovskite CaTiO_3 can reversibly accommodate substitution by Pt and Rh.^{13,15,16}

PGM substitutions are typically aliovalent and require the formation of charge-compensating oxygen vacancies, and in this regard, perovskite hosts are appealing because of their well-known robustness toward point defects. The mobility of oxide ions in bulk perovskites and oxygen storage and exchange capacities^{28–35} are associated with oxygen vacancies, and oxygen-deficient perovskites are well known to be excellent oxide ion conductors.^{36,37} Oxygen nonstoichiometry has been shown to significantly alter the activity of a variety of perovskites that catalyze the CO oxidation reaction.^{2,38–40} Prereduction of the double perovskites $\text{Ba}_2\text{FeNbO}_6$ and Ba_2CoWO_6 was found to lower the light-off temperature in CO oxidation under stoichiometric CO/O₂ conditions by 50–100 °C relative to the as-prepared materials with full oxygen stoichiometry.² In Pd-substituted BaCeO_3 , it has recently been shown that, under CO-rich conditions, a mechanism mediated by the host governs the reaction kinetics.⁴¹ The only reported nonperovskite complex oxide redox host for Pd^{2+} that displays egress/ingress behavior was described by us: metastable hexagonal $\text{YFe}_{1-x}\text{Pd}_x\text{O}_{3-\delta}$.¹⁸

Both YFeO_3 and YMnO_3 can be prepared as either perovskite or hexagonal variants (Figure 1); however, YFeO_3 is reported to be metastable in the hexagonal Be_3N_2 -type $P6_3/mmc$ structure,⁴² whereas YMnO_3 is metastable as perovskite.⁴³ The preference of

YMnO_3 for the hexagonal structure, relative to YFeO_3 's preference for perovskite, likely arises from the desire of Mn^{3+} to avoid a Jahn–Teller state by adopting trigonal bipyramidal coordination, which is a nondegenerate electronic configuration for high-spin d^4 cations. Fe^{3+} is also nondegenerate in the high-spin configuration for trigonal bipyramidal coordination, and Mn^{3+} and Fe^{3+} have identical Shannon–Prewitt ionic radii in 5-fold coordination.^{44,45} The absence of a center of symmetry in room-temperature YMnO_3 (space group $P6_3cm$) yields a ferroelectric material, and much work has addressed the magneto-electric properties of YMnO_3 .^{46,47} Recently, it was found that dilute amounts of Mn^{3+} in the $\text{YN}_{1-x}\text{Mn}_x\text{O}_3$ solid solution produce brilliant blue-colored powders, arising from a symmetry-allowed d–d transition, and shown that this can be extended more generally to trigonal bipyramidal Mn^{3+} in other structure types as well.^{48,49}

In the present work, the preparation and characterization of Pd-substituted $\text{YMn}_{0.5}\text{Fe}_{0.5}\text{O}_3$ are described. All attempts to introduce Pd^{2+} into the end-member YMnO_3 were unsuccessful, which led us to consider a solid solution between YFeO_3 and YMnO_3 as a host candidate. Phase evolution in amorphous sol–gel precursors of $\text{YMn}_{0.5}\text{Fe}_{0.5}\text{O}_3$ and Pd-substituted $\text{YMn}_{0.5}\text{Fe}_{0.5}\text{O}_3$, studied by in situ variable-temperature X-ray powder diffraction, is presented and compared with YMnO_3 , providing insight into why Pd substitution in YMnO_3 could not be achieved. Using synchrotron X-ray powder diffraction, X-ray photoelectron spectroscopy (XPS), and X-ray absorption spectroscopy, we show that Pd is dispersed as Pd^{2+} ions in the as-prepared $\text{YMn}_{0.5}\text{Fe}_{0.5-x}\text{Pd}_x\text{O}_{3-\delta}$ ($0 \leq x \leq 0.07$) materials. In contrast to $\text{YFe}_{1-x}\text{Pd}_x\text{O}_{3-\delta}$, $\text{YMn}_{0.5}\text{Fe}_{0.5-x}\text{Pd}_x\text{O}_{3-\delta}$ tolerates only a modest degree of redox cycling, with repeated cycles leading to the formation of PdO. The catalytic performance of $\text{YMn}_{0.5}\text{Fe}_{0.5-x}\text{Pd}_x\text{O}_3$ for the oxidation of CO to CO_2 under CO-lean conditions is nearly identical to that of $\text{YFe}_{1-x}\text{Pd}_x\text{O}_{3-\delta}$, both being comparable to $\text{PdO}/\text{Al}_2\text{O}_3$. The factors that differentiate $\text{YMn}_{0.5}\text{Fe}_{0.5-x}\text{Pd}_x\text{O}_{3-\delta}$ from perovskite-type host compounds are discussed, suggesting crystal chemical criteria for selecting other complex oxides that may offer improved efficacy toward redox cycling of the precious metal substituent and catalytic performance.

EXPERIMENTAL SECTION

Hexagonal $\text{YMn}_{0.5}\text{Fe}_{0.5}\text{O}_3$ and $\text{YMn}_{0.5}\text{Fe}_{0.5-x}\text{Pd}_x\text{O}_{3-\delta}$ were prepared using a sol–gel method. In a typical preparation, 5 mmol of

$\text{Y}(\text{NO}_3)_3 \cdot 6\text{H}_2\text{O}$ (Aldrich, 99.9%) was combined with 2.5 mmol of $\text{Mn}(\text{NO}_3)_2 \cdot x\text{H}_2\text{O}$ (Aldrich, 98%) and 2.5 mmol of $\text{Fe}(\text{NO}_3)_3 \cdot 9\text{H}_2\text{O}$ (Aldrich, 98+%) and dissolved in 20 mL of deionized water. A total of 20 mmol of citric acid, dissolved in 10 mL of DI H_2O (2:1 citrate/nitrate ratio), was added to the solution and the pH then neutralized with NH_4OH . For Pd-substituted samples, the appropriate molar amount of $\text{Pd}(\text{C}_2\text{H}_3\text{O}_2)_2$ was dissolved in 2 mL of reagent grade acetone and added dropwise to the sol, after pH adjustment, at 60 °C. Ethylene glycol was added as an additional complexing agent. The water was slowly evaporated at 75 °C, leaving a homogeneous gel, which was pyrolyzed at 350 °C for 2 h to give a fine black amorphous powder. The amorphous powders were ground thoroughly and heated at 800 °C for 10 h in zirconia crucibles to produce the black compounds.

Phase identification was performed with a Philips X'PERT diffractometer, and in situ variable-temperature diffraction was collected on a Bruker D8 diffractometer with an Anton Parr hot-stage, using $\text{Cu K}\alpha$ radiation. For the in situ X-ray thermodiffraction studies, samples were heated quickly (1 °C min^{-1}) to 700 °C, then at 10 °C min^{-1} between 700 and 1000 °C. The samples were held at each temperature for the duration of the collection times, 20 min. Synchrotron X-ray powder diffraction patterns were measured in transmission mode at room temperature on beamline 11-BM at the Advanced Photon Source, Argonne National Laboratory, with an X-ray wavelength of 0.412162 Å (about 30 keV). Samples were ground thoroughly in an agate mortar and packed in Kapton tubes. Additional details about the 11-BM diffractometer can be found at <http://11bm.xor.aps.anl.gov/>. Synchrotron X-ray powder diffraction patterns are shown in Q space (Å^{-1}); $Q = 4\pi \sin(\theta)/\lambda$. Rietveld refinements were performed using the XND code.⁵⁰ Bond valence analysis made use of the Bond Valence Calculator.⁵¹

X-ray photoelectron spectra were obtained on a Kratos Axis Ultra Spectrometer with a monochromatic Al $\text{K}\alpha$ source ($E = 1486$ eV). A charge neutralizer was used, and the angle between the detector and X-ray source was 54.7°. Powdered samples were mounted on a stainless steel sample holder using double-sided carbon tabs. The residual pressure inside the analysis chamber was below 7×10^{-9} Torr. Survey spectra over wide ranges of binding energy were acquired using an analyzer pass energy of 160 eV, and high-resolution spectra of Mn 2p, Fe 2p, Y 3d, and Pd 3d levels were acquired at a pass energy of 40 eV. Measured binding energies are accurate to ± 0.2 eV. Quantitative analysis was performed using photoionization cross sections from Scofield.⁵² Spectra were calibrated to the C 1s peak from adventitious hydrocarbon, expected at a binding energy of 285.0 eV. For peak fitting of spin-orbit doublets in the high-resolution scans of the Pd 3d levels, the peak area ratio of $d_{3/2}$ to $d_{5/2}$ was constrained to 2/3.

Extended X-ray absorption fine structure (EXAFS) measurements were made in transmission mode using Ar-filled ionization chambers at beamline 10-BM of the Materials Research Collaborative Access Team (MR-CAT) at the Advanced Photon Source located at Argonne National Laboratory. The spectrum of Pd foil was simultaneously collected for energy calibration to the Pd K edge (24.350 keV). A 75 mg sample was pressed into a 4 mm diameter pellet and placed in a six-position sample holder, which allows six samples to be treated under identical conditions. The sample holder was installed in a 30 cm \times 2.5 cm cylindrical quartz reactor with Cajon fittings and shut-off valves, sealed by O rings. The 0.5 mm \times 0.5 mm X-ray beam passed through Kapton windows at each end of the reactor and center of each sample for data acquisition. Spectra were recorded under a He atmosphere, and data were collected at room temperature for the samples $x = 0.05$ as-prepared, $x = 0.05$ reduced ex-situ at 500 °C in 5% H_2 , and $x = 0.05$ reoxidized ex-situ at 800 °C in pure O_2 . EXAFS data were extracted using the IFEFFIT 1.2.10 software package,⁵³ and the curve fit parameters were obtained using standard procedures, that is, least-squares fitting of the k^3 -weighted magnitude and imaginary part of the Fourier transform

of EXAFS oscillations. Analysis of the data was performed using the Artemis software⁵⁴ and utilized single scattering paths generated by FEFF6. The input models were constructed from the crystal structures of PdO ,⁵⁵ fcc-Pd , and the ordered intermetallic FePd .⁵⁶ EXAFS spectra were fit in the ranges of $k = 2.0\text{--}10.0$ Å^{-1} and $R = 1.0\text{--}3.5$ Å. The first Pd–O single scattering path in the PdO model was used to fit the first coordination shell in the spectra of both the as-prepared and the reoxidized materials. The amplitude reduction factor (S_0^2) was found by fitting the Pd foil spectrum and held fixed in all subsequent fits ($S_0^2 = 0.9$). The energy shift (ΔE_0), coordination number (N), mean-squared displacement (σ^2), and the bond length (R) were refined for the Pd–O single scattering path for the spectra of both the as-prepared and the reoxidized samples. In the reoxidized sample, two longer Pd–Pd paths were used to fit the second coordination shell with each path having its own refined N value, and σ^2 and R were constrained to have the same values in both paths. The spectrum of the reduced sample was modeled using two scattering paths, Pd–Pd and Pd–Fe. The value of ΔE_0 was refined as a global parameter. The values of N , σ^2 , and R were refined, with σ^2 constrained to the same value for both paths.

N_2 sorption isotherms were measured on a Micromeritics TriStar 3000 instrument at liquid nitrogen temperature. Prior to measurement, powder samples were degassed by heating overnight at 250 °C under flowing nitrogen. Surface areas were determined by application of Brunauer–Emmett–Teller (BET) theory,⁵⁷ and pore size distributions were calculated using the Barrett–Joyner–Halenda (BJH) method.⁵⁸ Secondary electron field emission scanning electron microscopy (SEM) was performed on a Sirion XL30 microscope. SEM samples were mounted on aluminum stubs using double-sided conductive carbon tapes. Carbon coating was applied to the samples prior to imaging.

Catalytic experiments were carried out in a Hiden CATLAB fixed-bed tubular quartz microreactor (18.50 cm \times 0.48 cm i.d.), located in a tubular furnace with temperature control between ambient temperature and 1100 °C. The catalyst (50 mg) was loaded into the reactor to give a bed length of ca. 1.0 cm, held in place with plugs of quartz wool. The temperature was monitored by a K-type thermocouple touching the catalyst bed. The oxidation of CO was studied as a temperature-programmed reaction, using a certified premixed 1000 ppm $\text{CO}/9.5\%$ O_2/Ar balance (Airgas, Inc.), at a flow rate of 50 mL min^{-1} . The operating pressure was 1 atm, and the pressure drop (<0.03 atm) was neglected. Product compositions were monitored with an online quadrupole mass spectrometer (HR-20, Hiden Analytical). The electron energy and emission current were set to 70.0 eV and 250 μA , respectively. A secondary electron multiplier (SEM) detector was used to monitor the MS signals at $m/z = 44$ (CO_2^+) and 28 (CO^+). The outlet concentration of CO_2 (ppm) was calculated from the signal at $m/z = 44$, using a premixed calibration gas containing 1000 ppm CO_2 balanced by N_2 . Because CO and CO_2 have a common ion at $m/z = 28$ (CO^+), the CO signal was corrected for the contribution from the ionization of CO_2 . The outlet concentration of CO was calculated from the remaining signal at $m/z = 28$, using a premixed calibration gas containing 1050 ppm CO balanced by He.

RESULTS

Preparation and Bulk Structure Characterization. $\text{YMn}_{0.5}\text{Fe}_{0.5}\text{O}_3$ and $\text{YMn}_{0.5}\text{Fe}_{0.5-x}\text{Pd}_x\text{O}_{3-\delta}$ were prepared by a citrate sol–gel method via an amorphous precursor obtained through pyrolysis of the gel. The gels were dried at 80 °C and heated at 350 °C for 2 h to remove the organic components, resulting in porous spongelike black powders. The precursors were thoroughly ground and heated in air at 800 °C for 10 h to yield black powders with an average crystalline correlation length (crystallite size) of 20 nm, estimated from Scherrer broadening. Adjustment of the sol pH to ~ 7 was essential for producing a single

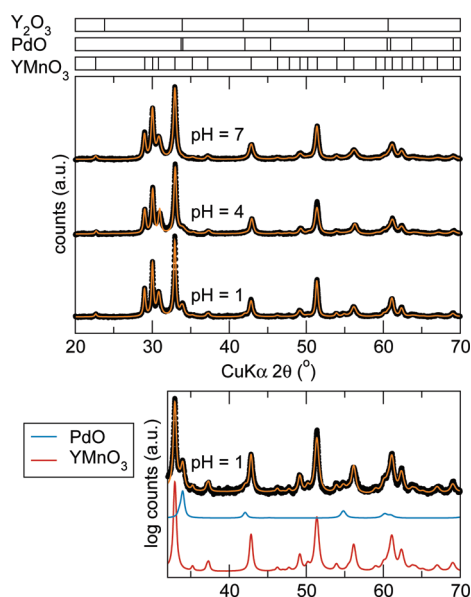


Figure 2. Powder X-ray diffraction patterns of $\text{YMn}_{0.5}\text{Fe}_{0.5-x}\text{Pd}_x\text{O}_{3-\delta}$ prepared from different sol pHs. The phase contributions for the sample prepared at pH = 1 are shown on a log scale. Despite the formation of PdO in samples prepared under acidic conditions, no reflections from Y_2O_3 are observed.

crystalline phase. In palladium-substituted samples, under acidic (pH = 1) and mildly acidic (pH = 4) conditions, a mixture of $\text{YMn}_{0.5}\text{Fe}_{0.5}\text{O}_3$ and PdO is obtained, with PdO clearly discernible in the powder X-ray diffraction patterns (Figure 2). No evidence for the formation of PdO is evident in samples prepared from a neutral (pH = 7) sol. Raising the pH of the solution facilitates deprotonation of the carboxylic acid groups in citric acid and favors complexation to the metal ions. When the pH exceeds 7, some precipitation of metal hydroxides occurs, preventing the formation of a homogeneous gel.

Variable-temperature in situ X-ray powder diffraction was used to monitor the phase evolution of YMnO_3 , $\text{YMn}_{0.5}\text{Fe}_{0.5}\text{O}_3$, and $\text{YMn}_{0.5}\text{Fe}_{0.45}\text{Pd}_{0.05}\text{O}_{3-\delta}$ amorphous sol–gel precursors, shown in Figure 3. YMnO_3 is poorly crystalline until 1000 °C, at which point the metastable perovskite phase dominates. All of our attempts to introduce Pd into YMnO_3 resulted in the formation of PdO, and this appears to be due to the higher temperatures needed to form the manganite. The partial substitution of Fe for Mn lowers the crystallization temperature, although a mixture of hexagonal $P6_3cm$ and orthorhombic $Pnma$ perovskite phases is present at 1000 °C. In contrast, the Pd-substituted material displays only the hexagonal phase, suggesting that Pd promotes its stabilization. Prolonged heating at temperatures above 800 °C leads to phase separation of both the unsubstituted and the Pd-substituted mixed Fe and Mn materials.

Rietveld refinements of high-resolution synchrotron X-ray powder diffraction data collected on $\text{YMn}_{0.5}\text{Fe}_{0.5-x}\text{Pd}_x\text{O}_{3-\delta}$ samples ($0 \leq x \leq 0.07$) are displayed in Figure 4. Size broadening effects are very pronounced in the observed diffraction profiles, and the patterns contain many overlapping reflections. Large diffuse scattering components are present in the background signals of all samples, suggesting a significant degree of structural disorder. Structure and refinement parameters are given in Table 1. Because of the lack of X-ray scattering contrast

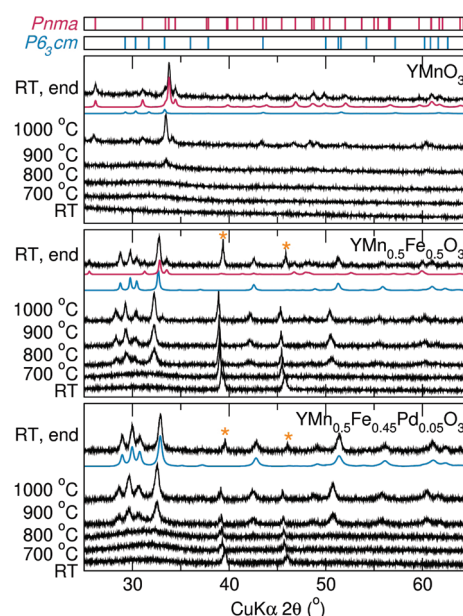


Figure 3. Variable-temperature X-ray diffraction showing the phase evolution of amorphous sol–gel precursors (pyrolyzed at 350 °C) for YMnO_3 (top), $\text{YMn}_{0.5}\text{Fe}_{0.5}\text{O}_3$ (middle), and $\text{YMn}_{0.5}\text{Fe}_{0.45}\text{Pd}_{0.05}\text{O}_{3-\delta}$ (bottom). YMnO_3 is not well crystalline until 1000 °C, and only a small fraction of the hexagonal form is present. Substituting some Fe for Mn lowers the temperature of crystallization, and further substituting some Pd for Fe stabilizes the hexagonal form. Rietveld refinements are shown in color for each sample, fit to the data collected after cooling to room temperature. Note that prolonged heating above 800 °C leads to phase separation of the mixed Mn–Fe compounds. Orange asterisks denote the position of reflections from the platinum hot stage, evident in the middle and bottom panels. The 2θ shifts of the Bragg reflections from the sample and hot stage are due to thermal expansion.

between Mn and Fe, site occupancies were fixed at the nominal values. Pd was assumed to occupy the trigonal bipyramidal B site. However, allowing the Pd occupancy to float led to unstable refinements, so its occupancy was also fixed at the nominal stoichiometric values. The possibility of Pd residing on a yttrium A site was also considered—despite this being very unlikely given the large (~ 0.3 Å) difference in the ionic radii of seven-coordinate Y^{3+} and four-coordinate Pd^{2+} —but led to both poor visual and statistical agreement relative to refinements in which Pd was located on the B site. Atomic displacement parameters (ADPs) were modeled isotropically, with all four oxygen atoms in the asymmetric unit constrained to have the same ADP value. The ADPs for the site-sharing Mn/Fe/Pd atoms were also constrained to have the same value.

For comparison, stable refinement of the Pd occupancy was possible even from lab (Cu K α) diffraction data for the $\text{YFe}_{1-x}\text{Pd}_x\text{O}_3$ series.¹⁸ The inability to refine the Pd occupancy in $\text{YMn}_{0.5}\text{Fe}_{0.5-x}\text{Pd}_x\text{O}_{3-\delta}$ samples may be related to the increased number of atomic positions needed to describe the YMnO_3 structure or structural disorder, or it could indicate that Pd does not reside precisely on the B site of the host but is displaced as seen in $\text{BaCe}_{1-x}\text{Pd}_x\text{O}_{3-\delta}$.¹⁷ Statistical measures of the refinements worsen with increasing substitution, in particular, R_{Bragg} , which is close to 9% for $x = 0.07$, although the visual agreement between the calculated and observed intensities remains strong. With increasing Pd content, the B site ADP steadily increases, which may arise from static disorder within the

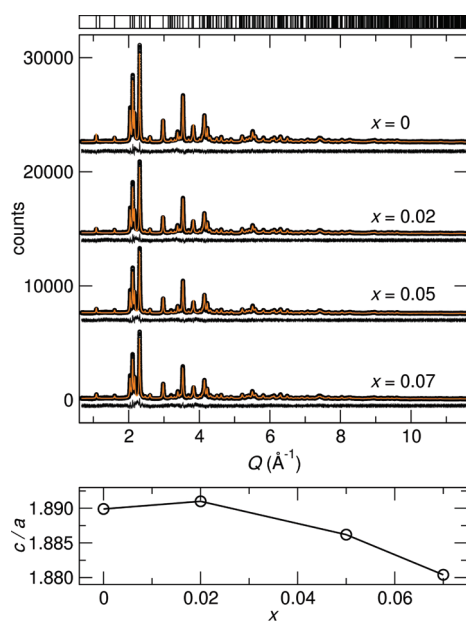


Figure 4. Synchrotron powder X-ray diffraction patterns of $\text{YMn}_{0.5-x}\text{Fe}_{0.5-x}\text{Pd}_x\text{O}_{3-\delta}$ ($0 \leq x \leq 0.07$) and corresponding Rietveld refinements (top). Evolution of the c/a lattice parameters ratio as a function of substitution level (bottom). Lines connecting the points are drawn for clarity. Error bars, not shown, are comparable to the width of the line connecting the data points.

materials. The difficulty in locating oxygen with X-rays when heavier elements are present is reflected in the chemically unreasonable bond valence sum of Y1, ≈ 4 , due to two unreasonably short bonds between Y1 and O1. We emphasize that the refinements reported here serve as evidence of the phase compositions of the samples but are not reliable models with respect to the anion positions.

Large improvements in the refinement statistics and visual agreement were made by introducing a preferred orientation correction, although this did not influence the structural parameters. Without the correction, $00l$ reflections were overestimated and $h00$ reflections underestimated. For the $x = 0$ sample, R_{Bragg} was reduced from near 10% to 5% by applying the correction, and similar improvements were found for the other samples. Considering the small sizes of crystallites in the samples, it is unusual that a preferred orientation correction had to be included in the refinements. Powder diffraction measurements on the 11-BM diffractometer were performed in transmission mode with samples contained in Kapton capillaries; given the layered nature of the hexagonal structure, the procedure of packing the samples into the capillaries appears to have produced a nonrandom assortment of crystallite orientations. Including preferred orientation corrections also improved the fit quality to laboratory X-ray diffraction data. Given the higher levels of noise in the lab X-ray data, however, these effects were less pronounced.

Weak reflections from orthorhombic YFeO_3 were apparent in the diffraction patterns for $x = 0$ and $x = 0.02$ samples, estimated at 3 and 4 mol %, respectively, from quantitative phase analysis. The addition of the perovskite phase made marginal improvements to the refinement statistics. The absence of the perovskite phase in samples with higher Pd contents suggests that the parent compound may be slightly Fe-deficient. Alternately, the stabilization of the hexagonal structure by Pd may be stronger with

Table 1. Results of Rietveld Refinements to Synchrotron X-Ray Diffraction Data on $\text{YMn}_{0.5}\text{Fe}_{0.5-x}\text{Pd}_x\text{O}_{3-\delta}$ Powders^a

parameters	$x = 0.00$	$x = 0.02$	$x = 0.05$	$x = 0.07$
R_p (%)	7.22	7.86	8.43	9.09
wR_p (%)	9.82	10.68	11.51	12.43
R_{Bragg} (%)	4.96	6.04	6.42	8.89
χ^2	1.69	1.70	1.75	1.98
a (Å)	6.1458(1)	6.1459(1)	6.1476(1)	6.1558(1)
c (Å)	11.6154(4)	11.6216(4)	11.5959(4)	11.5756(5)
V (Å ³)	379.9(1)	380.2(1)	379.5(1)	379.9(1)
Y1, z	0.2269(5)	0.2266(5)	0.2206(1)	0.2281(4)
Y2, z	0.2617(5)	0.2622(5)	0.2621(4)	0.2639(4)
Mn/Fe/Pd, x	0.3281(6)	0.3267(6)	0.3255(6)	0.3257(7)
O1, x	0.2959(10)	0.2921(11)	0.2922(12)	0.2866(14)
O1, z	0.3302(11)	0.3287(10)	0.3268(10)	0.3237(10)
O2, x	0.6526(11)	0.6549(13)	0.6496(13)	0.6557(17)
O2, z	0.1623(10)	0.1613(9)	0.1599(9)	0.1591(9)
O3, z	0.0094(10)	0.0053(10)	-0.0026(8)	-0.0059(10)
O4, z	0.4720(7)	0.4687(7)	0.4669(6)	0.4704(7)
Y1, U_{iso} (Å ²)	0.0060(5)	0.0075(6)	0.0092(6)	0.0131(7)
Y2, U_{iso} (Å ²)	0.0082(3)	0.0084(3)	0.0065(3)	0.0056(3)
Mn/Fe/Pd, U_{iso} (Å ²)	0.0062(2)	0.0080(2)	0.0096(3)	0.0146(4)
O, U_{iso} (Å ²)	0.0089(5)	0.0081(6)	0.0092(7)	0.022(1)

^a Note: The crystal structures are described in space group $P6_3cm$ (No. 185) with Y1 at $0,0,z$; Y2 at $1/3,2/3,z$; Mn/Fe/Pd at $x,0,z$; O1 and O2 at $x,0,z$; O3 at $0,0,z$; and O4 at $1/3,2/3,z$. Because all of the atoms in the asymmetric unit of the $P6_3cm$ structure are on Wyckoff positions that have variable z parameters, anchoring of the B site at $x,0,1/2$ was necessary to achieve convergence.

increases in the Pd/Fe ratio. Given that the substitution of Pd stabilizes the hexagonal forms of YFeO_3 ¹⁸ and $\text{YMn}_{0.5}\text{Fe}_{0.5}\text{O}_3$, it is unlikely that the perovskite in the $x = 0.02$ sample is Pd-substituted. There is no evidence for the presence of a $P6_3/mmc$ phase.

Refined structural parameters do not evolve smoothly across the series or follow the Vegard law. Because the substitution of Pd^{2+} for $(\text{Mn,Fe})^{3+}$ is not isovalent, and “ YPdO_3 ” does not exist, the Vegard law is not expected to be followed. Although the cell volume changes very little with (nominal) Pd content (in contrast to what would be expected for substitution of the larger Pd^{2+} (0.64 Å for CN = 4) for Fe^{3+} (0.58 Å for CN = 5)), the a edge tends to expand while the c edge contracts, although an increase in the c parameter was observed for $x = 0.02$. The c/a ratio across the series is plotted in the bottom panel of Figure 4, showing a generally decreasing trend.

Surface Composition. The relative surface cation ratios quantified from XPS survey scans of as-prepared samples in the $\text{YMn}_{0.5}\text{Fe}_{0.5-x}\text{Pd}_x\text{O}_{3-\delta}$ series are listed in Table 2 and suggest a somewhat Y-enriched surface. Y-enriched surfaces observed in metastable hexagonal $\text{YFe}_{1-x}\text{Pd}_x\text{O}_3$ ¹⁸ were explained on the basis of the high surface free energy of Y_2O_3 . Some evidence for a Y_2O_3 impurity was apparent from diffraction studies of the $\text{YFe}_{1-x}\text{Pd}_x\text{O}_{3-\delta}$ series,¹⁸ although it is not observed for $\text{YMn}_{0.5}\text{Fe}_{0.5-x}\text{Pd}_x\text{O}_{3-\delta}$. The total A site-to-B site cation ratios range from 3.0 to 2.5 times the expected bulk values. However, because surface compositions were not corrected for differing escape depths of photoelectrons for different elements, the amounts of Y and Pd relative to Mn and Fe are likely to be

overestimated. The Mn/Fe ratios are in good agreement with the nominal stoichiometry of the samples. Pd/Y ratios also agree well but are slightly higher than the nominal stoichiometry in the $x = 0.05$ and $x = 0.07$ samples, suggesting a slightly Pd-enriched surface.

Redox Cycling: Bulk and Surface Characterization. A series of reduction and reoxidation treatments were performed on $\text{YMn}_{0.5}\text{Fe}_{0.5-x}\text{Pd}_x\text{O}_{3-\delta}$ samples to evaluate the mobility of Pd and its change in state. Reduction was performed in flowing 5% $\text{H}_2/95\% \text{N}_2$ and oxidation in pure O_2 at 800°C . When heated in a reducing atmosphere above 200°C , Pd is extruded from the lattice as *fcc*-Pd⁰ metal, as evidenced by XRD and XPS. Partial reduction occurs up to 450°C , with complete reduction at 500°C . At temperatures above 600°C in the reducing atmosphere, the compounds were completely transformed to a mixture of the composite oxides and elemental metals (not shown).

Surface areas were determined by N_2 sorption measurements. The BET surface areas of the as-prepared, reduced, and reoxidized samples are plotted as a function of substitution level in Figure 5a, along with the pore size distribution (Figure 5b) for $x = 0$ as-prepared and $x = 0.05$ as-prepared, reduced, and reoxidized. The unsubstituted compound has a surface area around $22 \text{ m}^2 \text{ g}^{-1}$, whereas those of the Pd-containing samples range from 17 to $18 \text{ m}^2 \text{ g}^{-1}$. The surface areas of the substituted materials increase upon reduction, consistent with an increase in

porosity observed by electron microscopy (Figure 5c,d). Modest increases in the surface area of reoxidized samples were found for $x = 0.02$ and $x = 0.05$, though not in the $x = 0.07$ sample.

Synchrotron diffraction patterns for the following samples are shown in Figure 6: $x = 0.05$ as-prepared, $x = 0.05$ reduced at 500°C for 5 h, $x = 0.05$ reoxidized for 10 h at 800°C , and an $x = 0.07$ sample after three reduction/reoxidation cycles. Visually, the agreement between the calculated and observed intensities is more easily evaluated on a log scale, and the quality of these fits is representative of the quality of other refinements reported here. The Pd(111) reflection is the only peak associated with Pd that is not convoluted with Bragg peaks from the host. The refined lattice parameter of $3.850(2) \text{ \AA}$ is about 1% smaller than that of elemental Pd bulk metal, a point that will be further discussed

Table 2. Surface Atomic Ratios of Cations in As-Prepared Hexagonal $\text{YMn}_{0.5}\text{Fe}_{0.5-x}\text{Pd}_x\text{O}_{3-\delta}$ ^a

sample	Y 3s (%)	Mn 2p _{3/2} (%)	Fe 2p _{3/2} (%)	Pd 3d _{5/2} (%)	Pd/Y (%)
$x = 0$	75.0	11.2	13.8	0	
$x = 0.02$	73.8	10.4	14.2	1.6	2.1
$x = 0.05$	73.3	11.3	10.8	4.6	6.3
$x = 0.07$	71.2	11.5	11.0	6.3	8.8

^aNote: surface compositions are uncorrected for differing escape depths of photoelectrons from different elements.

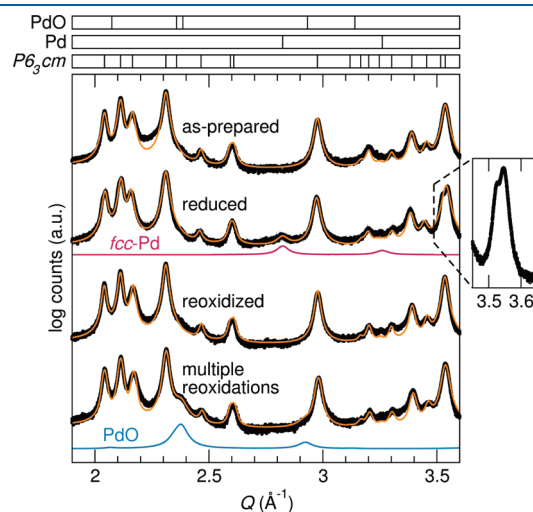


Figure 6. Synchrotron powder X-ray diffraction patterns and corresponding Rietveld refinements, plotted on a log scale, for $x = 0.05$ as-prepared, reduced, and reoxidized, and $x = 0.07$ after three reduction/reoxidation cycles. The inset displays a region from the diffraction pattern of the reduced sample where peak splitting is clearly evident.

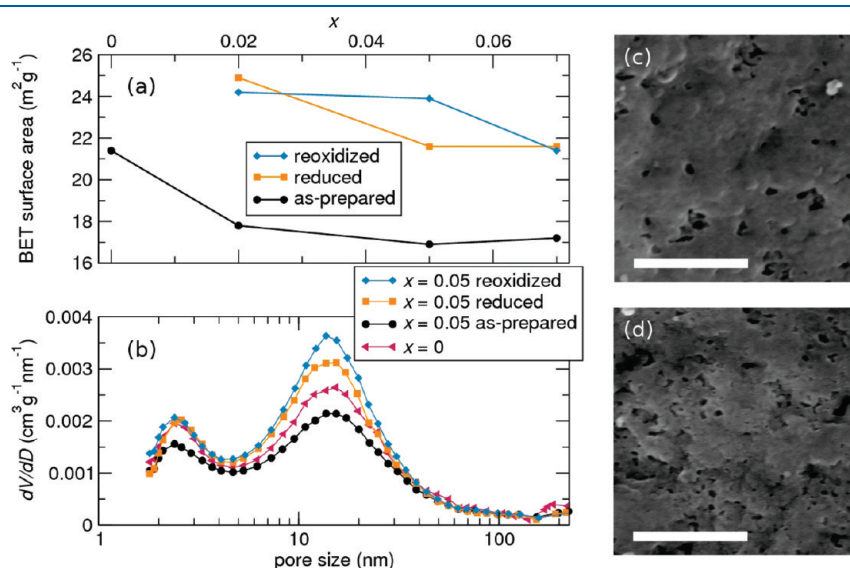


Figure 5. (a) BET surface area of as-prepared, reduced, and reoxidized samples. (b) Pore size distribution of $x = 0$ and $x = 0.05$ as-prepared, reduced, and reoxidized. (c, d) Representative scanning electron micrograph images of $x = 0.07$ as-prepared (c) and after reduction (d). The scale bars correspond to 500 nm.

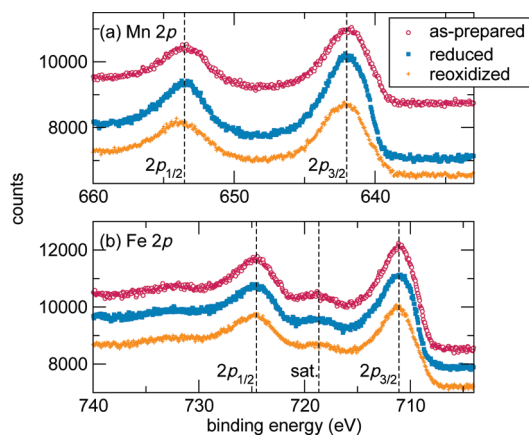


Figure 7. High-resolution XPS of the Mn 2p and Fe 2p regions in $x = 0.05$ as-prepared, $x = 0.05$ reduced at $500\text{ }^{\circ}\text{C}$, and $x = 0.05$ reoxidized at $800\text{ }^{\circ}\text{C}$.

with respect to X-ray absorption spectroscopy data collected on the same $x = 0.05$ sample. Quantitative analysis of the phase fractions in the reduced sample gives an estimate of the molar fraction of Pd to be 4.9%, in excellent agreement with the nominal stoichiometry of the as-prepared material. Quantitative analysis of the reduced $x = 0.07$ sample gives an estimate of the Pd phase fraction at 6.6%. The refined lattice parameter for Pd in the reduced $x = 0.07$ sample is the same as that of the Pd in the reduced $x = 0.05$ sample within error. The particle size of the *fcc* Pd phase, estimated from Scherrer broadening, is 10 nm in both samples. The strongest reflection of PdO (101) occurs near 2.4 \AA^{-1} , and a small amount of intensity is observed here in all of the as-prepared materials, including the unsubstituted material. Only after repeatedly reducing and reoxidizing a Pd-substituted sample does a reflection unambiguously consistent with PdO appear.

Significant changes in the diffraction profiles were apparent in the reduced samples, with peak splitting observed in the $x = 0.05$ sample for the 110, 300, 304, 222, 334, and $41(2l)$ reflections. Such splitting can be seen at about 3.5 \AA^{-1} in the reduced sample, shown in the inset of Figure 6. In the $x = 0.07$ sample, the $10(2l)$ and $2k6$ reflections were dramatically weakened in intensity. The 302 and 312 reflections were observed to weaken for $x = 0.05$, but not for $x = 0.07$. Diffraction profiles indistinguishable from those of the as-prepared materials are restored upon reoxidation.

Similar changes in the unit cell volume were found for both unsubstituted and Pd-substituted samples, increasing upon reduction by 1% and contracting back to the same volume as the as-prepared samples when reoxidized. Both the *a* and the *c* lattice constants of $\text{YMn}_{0.5}\text{Fe}_{0.5}\text{O}_3$ and $\text{YMn}_{0.5}\text{Fe}_{0.5-x}\text{Pd}_x\text{O}_{3-\delta}$ were found to increase, although to a larger degree in the *ab* plane. $\text{YFe}_{1-x}\text{Pd}_x\text{O}_{3-\delta}$ also showed a volume increase upon reduction, but while the *ab* plane was found to expand, the *c* axis contracted. The lattice expansion can be explained by increasing cation–cation repulsion associated with the loss of lattice O, and also by the increase in ionic radii that accompanies the reduction of Mn^{3+} and/or Fe^{3+} to Mn^{2+} and Fe^{2+} . It is important to point out, however, that the radius increases would be rather large—the Shannon–Prewitt radii for four- and five-coordinate Mn^{2+} are 0.66 \AA and 0.75 \AA , respectively, representing 47% and 116% volume expansions. An ionic radius value has not been reported for trigonal bipyramidal Fe^{2+} . Despite the slightly smaller size expected for Fe cations relative to Mn due to increased effective

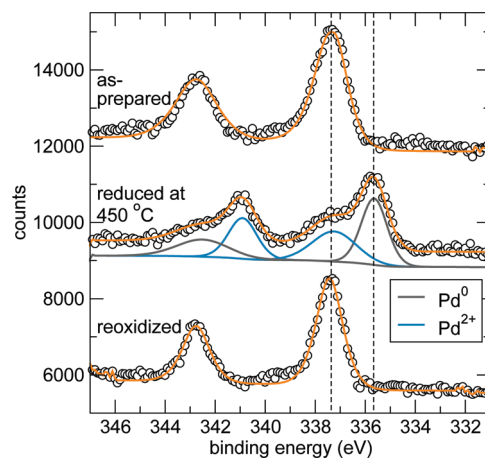


Figure 8. High-resolution XPS of the Pd 3d region in $\text{YMn}_{0.5}\text{Fe}_{0.43}\text{-Pd}_{0.07}\text{O}_{3-\delta}$ as-prepared, reduced at $450\text{ }^{\circ}\text{C}$, and reoxidized. The $x = 0.07$ composition is shown here rather than $x = 0.05$ because of the improved signal-to-noise ratios from the more heavily substituted phases. Up to $450\text{ }^{\circ}\text{C}$, Pd^{2+} is only partially reduced to Pd^0 .

nuclear charge, five-coordinate Fe^{2+} is still likely to be significantly larger than tetrahedral and square-planar Fe^{2+} , 0.63 \AA and 0.64 \AA , respectively, which are approximately 30% more voluminous than five-coordinate Fe^{3+} . The nearly identical radii of high-spin Mn^{3+} and Fe^{3+} are presumably due to an expansion associated with population of the d_{z^2} orbital in Fe^{3+} , counteracting the contraction that accompanies the larger effective nuclear charge. Thus, the modest observed volume expansion suggests that the host may tolerate only a small degree of reduction to Fe^{2+} or Mn^{2+} . It is interesting to note that high-spin Fe^{2+} is Jahn–Teller-active in trigonal bipyramidal coordination, whereas Mn^{2+} (isoelectronic with Fe^{3+} , high-spin d^5) is not. The origin of the peak-splitting observed in diffraction profiles of reduced samples could, in this light, be associated with a lattice distortion due to the presence of some Fe^{2+} species.

High-resolution XPS of the Mn and Fe 2p levels in the as-prepared, reduced, and reoxidized samples is shown in Figure 7. The spectra are broad due to the complicated multiplet splitting patterns that arise from spin–orbit coupling between core holes and unpaired valence electrons.^{59–62} The data are not of sufficient quality to unambiguously deconvolute the component multiplet signals, but the maxima, located at 641.9 eV for Mn $2p_{3/2}$ and 710.9 eV for Fe $2p_{3/2}$, are consistent with values reported for Mn^{3+} and Fe^{3+} .^{59,63–65} The satellite observed in the Fe XP spectra at 718.9 eV is a diagnostic signature of Fe^{3+} .⁶⁶ There are subtle changes in the line shapes observed for the reduced sample, with the Mn 2p signal becoming somewhat sharper, while the Fe 2p signal is slightly broadened. The maxima, however, remain centered at the same values as the as-prepared samples. Energy differences between Mn $2p_{3/2}$ signals for Mn^{2+} , Mn^{3+} , and Mn^{4+} are known to be rather small and difficult to deconvolute among the many multiplet contributions,^{64,65} making it difficult to definitively determine whether the spectrum of the reduced sample contains a contribution from Mn^{2+} . In contrast, resolution of Fe^{2+} from Fe^{3+} is typically more tractable due to the large shift of the satellite feature from ca. $+8\text{ eV}$ relative to the $2p_{3/2}$ maxima in Fe^{3+} to ca. $+6\text{ eV}$ in Fe^{2+} .⁶⁶ No discernible shift or weakening of the satellite feature is observed in the Fe 2p region of the reduced sample, suggesting the presence of only Fe^{3+} , though the slight broadening of the $2p_{3/2}$ feature to the low

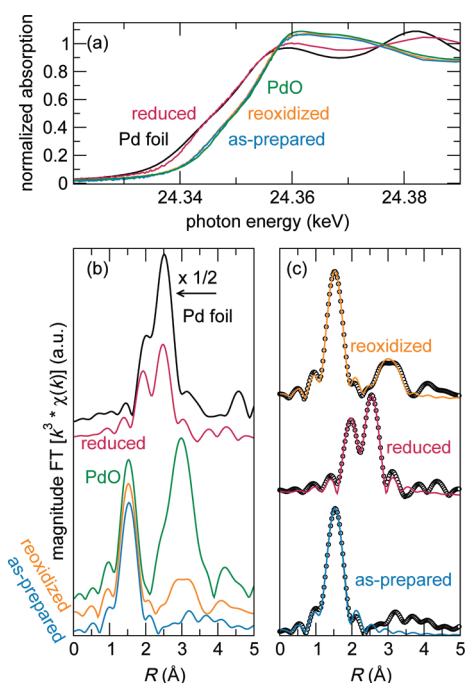


Figure 9. (a) Pd K-edge XANES and (b) FT-EXAFS spectra of $x = 0.05$ as-prepared, reduced at 500 °C, and reoxidized at 800 °C, compared with PdO and Pd foil. (c) FT-EXAFS spectra and fits for $x = 0.05$ as-prepared, $x = 0.05$ reduced at 500 °C, and $x = 0.05$ reoxidized at 800 °C. Note that distances are not corrected for the scattering phase shift.

binding energy side may implicate a small amount of Fe^{2+} . The Mn and Fe 2p signals of the reoxidized samples are also consistent with the as-prepared materials, with the exception that the Mn 2p_{1/2} signal appears to be slightly shifted and broadened to the high binding energy side. Further investigation is required to determine whether the oxidation states of Mn and Fe are changing during reduction and reoxidation.

High-resolution XPS spectra of the Pd 3d region for $\text{YMn}_{0.5}\text{Fe}_{0.43}\text{Pd}_{0.07}\text{O}_3$ as-prepared, reduced at 450 °C, and reoxidized are shown in Figure 8. The Pd 3d_{5/2} binding energy of 337.3 eV in the as-prepared and reoxidized samples is consistent with those reported for Pd-substituted YFeO_3 and indicates a slightly more ionic environment than Pd^{2+} in PdO, located at 336.9 eV in a commercial sample of bulk PdO. The presence of Pd^{2+} in the reduced phase is interpreted to result from incomplete reduction. Exposure to the air during the process of transferring the reduced sample to the XPS chamber could also result in partial oxidation of the surface of Pd^0 . Spectra for the $x = 0.07$ samples are shown here, rather than $x = 0.05$, because of the improved signal-to-noise ratios in the more heavily substituted phases. Complete reduction to Pd^0 at 500 °C is confirmed by the X-ray absorption studies described below and supported by the quantitative phase analysis of synchrotron X-ray diffraction data.

Pd K-edge X-ray absorption spectra were recorded ex-situ for $x = 0.05$ as-prepared, reduced at 500 °C, and reoxidized. XANES spectra are shown in Figure 9a with PdO and Pd foil standards for comparison. The XANES edge position and shape of the as-prepared and reoxidized materials are nearly identical to the shape found for PdO, showing a subtle shoulder on the low-energy side of the edge arising from weak transitions from the 1s to 5p nonbonding states.⁶⁷ The similar shapes of the absorption edge in as-prepared and reoxidized $\text{YMn}_{0.5}\text{Fe}_{0.45}\text{Pd}_{0.05}\text{O}_{3-\delta}$

Table 3. Optimized Parameters Obtained by EXAFS Analysis at the Pd K Edge ($S_0^2 = 0.9$)

sample	path	<i>N</i>	<i>R</i> (Å)	σ^2 (Å ²)	ΔE_0 (eV)
$x = 0.05$ as-prepared	Pd–O	4.1(5)	2.019(8)	0.003(1)	8.4(14)
$x = 0.05$ reduced	Pd–Pd	5.8(9)	2.67(1)	0.009(1)	0.20(1)
	Pd–Fe	1.7(4)	2.61(1)	0.009(1)	
$x = 0.05$ reoxidized	Pd–O	3.7(3)	2.012(5)	0.002(1)	7.6(11)
	Pd–Pd(1)	1.3(7)	3.023(9)	0.007(3)	
	Pd–Pd(2)	2.6(12)	3.412(9)	0.007(3)	

compared to the spectrum of PdO suggest that Pd is present as symmetric four-coordinate square planar Pd species in each of these materials. The absorption edge of the reduced sample is shifted to lower energy, consistent with the reduction of Pd^{2+} to Pd^0 , though the shape of the features beyond the edge are distinct from Pd foil.

Fourier transformed k^3 -weighted EXAFS spectra for the $x = 0.05$ samples, PdO, and Pd foil are shown in Figure 9b, and *R*-space fits to the total magnitude appear in Figure 9c. Fit parameters are listed in Table 3. The first coordination shell of the as-prepared and reoxidized samples is best fit by Pd surrounded by four O's, although the average coordination number of 4.5 that would be expected from the removal of one lattice O for every two substituted Pd atoms is within the error of the fit. Attempts to fit the data with a model based on the $\text{YMn}_{0.5}\text{Fe}_{0.5}\text{O}_3$ host with Pd residing on the B site were inconsistent with the observed data due to the absence of the large expected contributions at high *R* from longer scattering paths to Y and Mn/Fe. If Pd were present as PdO in the as-prepared sample, evidence of Pd–Pd correlations should be observed, as is the case for the reoxidized material. The absence of any well-defined higher-order coordination shell features indicates significant static local disorder around Pd, or a distribution of coordination sites. In calculations based on the host, the weakness of the longer scattering path contributions could only be accounted for by allowing unphysical, large values of σ^2 . The relatively small differences between Pd–O bond lengths in a model based on the B site of the host led to highly correlated parameters; if the differences in the bond distances are smaller than the resolution of a data set, it is not meaningful to fit them as separate paths. Thus, we chose to model the as-prepared material based on PdO, with a single Pd–O scattering path. Presumably, were Pd^{2+} incorporated on a well-defined site in the host lattice, some evidence of higher-order correlations would be evident in the EXAFS data.

It is clear from the XANES and FT-EXAFS data that the reduced sample is different than bulk Pd, containing a prominent scattering feature at lower *R*. This is best modeled as an alloy of Pd and Fe or Mn, the 3d metals being difficult to distinguish due to their similar X-ray scattering factors. A Pd–Fe alloy may be more likely, since Pd and Fe are well known to form bimetallic nanoparticles,^{68–70} while reports of nanoparticulate alloys between Pd and Mn are relatively scarce,⁷¹ although we have no direct evidence favoring one over the other. We chose to model the Pd-containing phase in the reduced material as a Pd–Fe phase, but modeling the alloy as a Pd–Mn phase would not influence the refined parameters.

Alloying between Pd and smaller Fe or Mn atoms may explain the small observed decrease in the lattice parameter of the *fcc* phase in reduced samples (ca. 1%) relative to pure Pd metal.

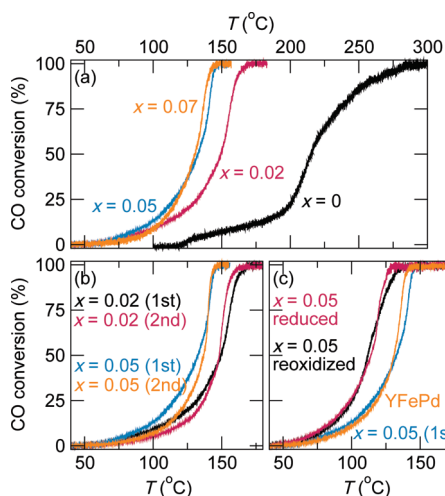


Figure 10. Light-off profiles for CO oxidation (1000 ppm CO in 10% O_2) over (a) fresh $YMn_{0.5}Fe_{0.5-x}Pd_xO_{3-\delta}$ with different levels of Pd substitution ($x = 0, 0.02, 0.05$, and 0.07); (b) fresh and reused $YMn_{0.5}Fe_{0.5-x}Pd_xO_{3-\delta}$, with $x = 0.02$ and 0.05 ; and (c) as-prepared (fresh), reduced, and reoxidized $YMn_{0.5}Fe_{0.45}Pd_{0.05}O_{3-\delta}$ and fresh $YFe_{0.95}Pd_{0.05}O_3$, denoted as YFePd.

The refined Pd–Fe coordination number is 1.7(4) at a bond distance of 2.61 Å, and the Pd–Pd coordination number is 5.8(9) at 2.67 Å. The fit parameters indicate the formation of Pd-rich bimetallic nanoparticles. The combined first shell average coordination numbers for the alloy phase are significantly less than what would be expected for 10 nm *fcc* crystallites—for which the average coordination number would be nearly 12 given the small fraction of atoms at the surface—suggesting the presence of particles smaller than the size estimated from Scherrer broadening. Because Bragg scattering is proportional to the scattering volume of particles, diffraction is insensitive to small particles in the presence of larger particles. EXAFS, on the other hand, is a number-averaged technique, yielding information about all of the species of the probed element present in the ensemble.

Catalytic Oxidation of CO. The ability of $YMn_{0.5}Fe_{0.5-x}Pd_xO_{3-\delta}$ to catalyze CO oxidation was evaluated in a feed of 1000 ppm CO in excess O_2 (10%, N_2 balance), to mimic the oxidizing conditions in the exhaust gas of lean-burn diesel engines. Light-off profiles, which track the conversion of CO to CO_2 as a function of temperature, are shown in Figure 10a for the fresh catalysts containing $x = 0, 0.02, 0.05$, and 0.07 . The Pd-free material gives a gradual, irregularly shaped, light-off curve reaching 50% conversion (T_{50}) at ca. 215 °C. In contrast, the profiles for the Pd-containing samples have a more conventional shape, with sharply increasing conversion above 50%, reflecting CO desorption necessary for O_2 activation. This behavior is characteristic of the CO inhibition that is usually observed for metallic catalysts and caused by strong CO adsorption on the active sites that prevents O_2 activation. The presence of just 2 atom % Pd substitution on the Fe site reduces T_{50} to 150 °C; however, further incorporation of Pd results in little improvement: catalysts containing 5 and 7 atom % Pd have comparable activities, with a T_{50} of ca. 140 °C. Synchrotron X-ray diffraction patterns collected after catalysis showed no changes from the as-prepared samples.

When the fresh catalysts are reused, the second light-off profiles are slightly different, Figure 10b. Although the T_{50} values are similar, activity is suppressed at low temperature in the reused

catalysts and increases slightly faster above T_{50} than for the fresh catalysts. These observations suggest that CO inhibition of the used catalyst is more severe, due to structural changes induced during the first experiment. Presumably, Pd^{2+} ions are extruded from the $YMn_{0.5}Fe_{0.5}O_3$ lattice under reaction conditions, then reduced by CO to form Pd^0 crystallites, or a PdFe alloy, as suggested by EXAFS.

The activity of $YMn_{0.5}Fe_{0.45}Pd_{0.05}O_{3-\delta}$ in CO oxidation is very similar to that of $YFe_{0.95}Pd_{0.05}O_{3-\delta}$ (Figure 10c). Also shown in Figure 10c is the effect of redox cycling; the light-off curve of as-prepared (fresh) $YMn_{0.5}Fe_{0.45}Pd_{0.05}O_{3-\delta}$ is compared to those recorded after the material was reduced, and after it was subsequently reoxidized. Reduction causes T_{50} to decrease to 110 °C, and it did not increase upon reoxidation of the catalyst. The improved activity of the reduced sample may be associated with its increased surface area, which persists in the reoxidized material. It is also possible that the extruded Pd is not completely reincorporated into the mixed oxide lattice upon reoxidation and is rapidly reduced under reaction conditions.

DISCUSSION

Preparation and Pd Substitution. Samal et al. reported preparation of the $YMn_{1-x}Fe_xO_3$ solid solution by a sol–gel process similar to the one employed in the present work.⁷² The $YMnO_3$ structure was observed up to $x = 0.3$, with a mixture of $YMnO_3$ and orthorhombic perovskite for the $x = 0.5$ composition. Their samples, however, were prepared at 900 °C. From our study, it is clear that the temperature window in which the $x = 0.5$ composition can be prepared is quite narrow, and that this phase is metastable. Prolonged heating of our samples at 900 °C results in phase separation.

The incorporation of Pd into $YMn_{0.5}Fe_{0.5}O_3$ requires neutralization of the sol pH, presumably to deprotonate the carboxylic acid groups of the citric acid chelating agent for coordination to Pd^{2+} ions in solution. The crystallization of PdO in samples prepared under acidic conditions indicates that pH adjustment enables Pd to remain well dispersed during pyrolytic formation of the amorphous precursor. The absence of detectable PdO in samples prepared from a sol at pH ~ 7 is consistent with isolated ions embedded in the oxide. The argument that small PdO clusters—smaller than can be detected by XRD—are present is inconsistent with preparation at 800 °C, at which temperature such clusters would readily ripen. Interestingly though, we see no direct evidence from the synchrotron diffraction studies that Pd incorporates on the B site of $YMn_{0.5}Fe_{0.5}O_3$, in contrast to $YFe_{1-x}Pd_xO_3$, for which the Pd occupancy was stably refined from both laboratory X-ray and neutron powder diffraction data.¹⁸ The absence of long-range correlations in the FT-EXAFS spectrum of $YMn_{0.5}Fe_{0.45}Pd_{0.05}O_{3-\delta}$ suggests that Pd does not occupy a well-defined site but rather is disordered throughout the lattice, or occupies a distribution of coordination sites. No X-ray absorption studies have been reported on $YFe_{1-x}Pd_xO_{3-\delta}$ for comparison. In contrast to the perovskite structure, $YMnO_3$ and $YFeO_3$ are not close-packed, and there may be sufficient space to accommodate a square planar PdO_4 unit—the most common geometry for d^8 cations—in a defect or interstitial site, despite such a site being difficult to envision geometrically. Ab initio modeling of Pd in $YMnO_3$ and $YFeO_3$ could provide insight into how the hexagonal structures incorporate Pd, and whether the lower symmetry of $YMnO_3$ influences the dopant geometry. A recent theoretical investigation of Pd and Pt substitution in

CeO₂ demonstrates that these divalent dopants prefer to sit off the ideal Ce lattice site in a position that enables square planar coordination to prevail, a consequence of the large crystal field stabilization energy.⁷³

A number of X-ray absorption studies have been reported for Pd-substituted perovskites,^{5,8,9,15,74–76} including in situ observations of the egress/ingress process in PGM-substituted perovskite hosts.^{14,77,78} In a recent XAS study by Eysler et al., the XANES spectra of LaFe_{1-x}Pd_xO₃, LaFeO₃ prepared in the presence of excess Pd, and a Pd-impregnated sample of LaFeO₃ were compared.⁹ Evidence of Pd substitution was present in all samples, though less so in the impregnated sample, identified by distinct XANES edge features consistent with distorted octahedral geometry around Pd. It is interesting to note that the FT-EXAFS spectrum reported for LaFe_{1-x}Pd_xO₃ does not contain intense higher shell features. For comparison, LaCo_{1-x}Pd_xO₃ has prominent Pd–La contributions in its FT-EXAFS spectrum.⁸ The FT-EXAFS spectrum of BaCe_{1-x}Pd_xO₃ also displays well-defined higher-order correlations.⁴¹

Redox-Driven Movement of Pd. Compared with bulk and supported PdO, YMn_{0.5}Fe_{0.5}O₃ stabilizes the Pd²⁺ oxidation state to higher temperatures, demonstrated by the persistence of Pd²⁺ in samples reduced at temperatures up to 450 °C. This is attributed to the presence of electropositive cations in the host and serves as evidence that Pd is dispersed in the oxide, rather than present as PdO on the surface of as-prepared samples. PdO deposited on CeO₂ is fully reduced below 100 °C in 5% H₂.⁷⁹ While the host offers stability to the substituent, the driving force to reincorporate as ions after being expelled as Pd⁰ nanoparticles appears to be rather low. YMn_{0.5}Fe_{0.5}O₃ is notably less effective at reincorporating Pd²⁺ than hexagonal YFeO₃.¹⁸ Reoxidation of Pd in YMn_{0.5}Fe_{0.5}O₃ requires rather high temperatures and does not lead to complete redispersion of Pd ions, whereas in the case of YFeO₃, reoxidation at 500 °C is sufficient to fully reincorporate Pd ions in the host.

Though many questions about the specifics of the YMn_{0.5}Fe_{0.5-x}Pd_xO_{3-δ} system remain to be addressed in future work, the present study raises some important questions apropos the preparation of new and improved PGM-substituted complex oxide host materials. It is clear that not all hosts are good hosts. Thus, we are led to ask the following: what are the crystal chemical conditions that facilitate reversible extrusion and reincorporation of PGM ions in complex oxides? Certainly a host consisting of highly electropositive cations is an important requisite, providing the driving force to stabilize PGM ions in oxide environments. In addition to stabilization, however, a good host must also present a sufficient driving force for PGM metal to *reincorporate* as ions. The factors that influence this ability are by no means fully elucidated, but one must infer that there is something distinctly different about YFe_{1-x}Pd_xO₃ as compared to YMn_{0.5}Fe_{0.5-x}Pd_xO₃ that accounts for their different abilities to reintegrate palladium into the respective hosts.

Catalytic Oxidation of CO. As-prepared YMn_{0.5}Fe_{0.5-x}Pd_xO_{3-δ} samples show similar light-off temperatures irrespective of the level of Pd substitution, as does YFe_{1-x}Pd_xO₃.¹⁸ This is contrasted with perovskite BaCe_{1-x}Pd_xO₃, for which the light-off temperature decreases significantly as a function of Pd concentration.⁸⁰ Whereas one oxygen vacancy is formed for every two Pd atoms substituted into the hexagonal hosts, a vacancy is formed for each Pd atom in BaCeO₃, confirmed by neutron diffraction.¹⁷ It was shown through a combination of density functional modeling and neutron pair distribution function analysis,^{17,80} and more recently using EXAFS,⁴¹

that the vacancy sits adjacent to Pd in the BaCeO₃ lattice, leaving Pd square planar next to a five-coordinate square pyramidal Ce. The uncertainty about the local Pd environment in YFeO₃ and YMn_{0.5}Fe_{0.5}O₃ prevents a direct comparison with BaCeO₃. However, the extent to which the differing polyhedral connectivities of the hosts promote oxygen mobility may explain the difference in activities as a function of substitution level. Oxide ion conduction occurs in both oxygen-deficient layered perovskites⁸¹ as well as those containing excess oxygen in interstitials,⁸² suggesting that the lowered dimensionality of the layered hexagonal materials is not responsible for the low mobility. To our knowledge, there are no reports in the literature of high oxygen mobility (oxide ion conductivity) in oxides that adopt the Be₃N₂ or related structures containing corner-connected trigonal bipyramids. This is consistent with the hypothesis that YFeO₃ and YMn_{0.5}Fe_{0.5}O₃ do not promote catalytic oxidation of CO by substituted Pd. Detailed mechanistic studies of the activity under a range of conditions are necessary to determine whether or not the hexagonal hosts mobilize oxygen.

CONCLUSIONS

A sol–gel route was developed for the preparation of YMnO₃-type YMn_{0.5}Fe_{0.5}O₃ and YMn_{0.5}Fe_{0.5-x}Pd_xO_{3-δ}. YMn_{0.5}Fe_{0.5}O₃ accommodates the substitution of Pd²⁺; however, the location of Pd in the host lattice is poorly defined: X-ray absorption spectroscopy at the Pd K edge suggests a symmetric four-coordinate Pd species whose local environment resembles PdO. While the related compound YFeO₃ has been shown to serve as a reversible redox host for Pd²⁺, YMn_{0.5}Fe_{0.5-x}Pd_xO_{3-δ} is much less capable of supporting this behavior. Repeated redox cycling of the substituted materials leads to the formation of PdO, which becomes readily evident by diffraction. As a catalyst for the oxidation of CO, YMn_{0.5}Fe_{0.5-x}Pd_xO_{3-δ} is effectively indistinguishable from YFe_{1-x}Pd_xO_{3-δ}, both of which perform similarly to PdO/Al₂O₃. This finding demonstrates that some host lattices are ineffective at enhancing catalytic activities and may serve effectively as inert supports. We hypothesize that the hexagonal hosts, consisting of layers of corner-connected trigonal bipyramids, do not present labile oxygen, that is, that the polyhedral connectivity does not accommodate transportation of oxide ions through the lattice.

AUTHOR INFORMATION

Corresponding Authors

*E-mail: sscott@engineering.ucsb.edu (S.L.S.), seshadri@mrl.ucsb.edu (R.S.).

ACKNOWLEDGMENT

The authors thank the Department of Energy, Office of Basic Energy Sciences, for supporting this work through Grant DE-FG02-10ER16081. Use of the Advanced Photon Source was supported by the U.S. Department of Energy, Office of Science, Office of Basic Energy Sciences, under Contract No. DE-AC02-06CH11357. Materials Research Collaborative Access Team (MRCAT, Sector 10 ID) operations are supported by the Department of Energy and the MRCAT member institutions. J.A.K. and R.D. thank the ConvEne IGERT Program (NSF-DGE 0801627) for support. C.R.P. acknowledges the CISEI program, supported by the Materials Research Laboratory (MRL) and the International Center for Materials Research. The use of MRL

Central Facilities are supported by the MRSEC Program of the NSF under Award No. DMR05-20415, a member of the NSF-funded Materials Research Facilities Network (www.mrfln.org).

REFERENCES

- (1) Voorhoeve, R. J. H.; Remeika, J. P.; Matthias, B. T.; Freeland, P. E. *Science* **1972**, *177*, 353–354.
- (2) Voorhoeve, R. J. H.; Trimble, L. E.; Khattak, C. P. *Mater. Res. Bull.* **1974**, *9*, 655–666.
- (3) Voorhoeve, R. J. H.; Remeika, J. P.; Trimble, L. E. *Ann. N. Y. Acad. Sci.* **1976**, *272*, 3–21.
- (4) Voorhoeve, R. J. H.; Johnson, D. W.; Remeika, J. P.; Gallagher, P. K. *Science* **1977**, *195*, 827–833.
- (5) Nishihata, Y.; Mizuki, J.; Akao, T.; Tanaka, H.; Uenishi, M.; Kimura, M.; Okamoto, T.; Hamada, N. *Nature* **2002**, *418*, 164–167.
- (6) Tanaka, H.; Taniguchi, M.; Kajita, N.; Uenishi, M.; Tan, I.; Sato, N.; Narita, K.; Kimura, M. *Top. Catal.* **2004**, *30–31*, 389–396.
- (7) Manjunath, B. B.; Tinku, B.; Shivakumara, C.; Vasanthacharya, N. Y.; Hegde, M. S.; Madras, G. *Appl. Catal., B* **2008**, *84*, 474–481.
- (8) Chiarello, G. L.; Grunwaldt, J.-D.; Ferri, D.; Krumeich, R.; Oliva, C.; Forni, L.; Baiker, A. *J. Catal.* **2007**, *252*, 127–136.
- (9) Eysler, A.; Mandaliev, P.; Winkler, A.; Hug, P.; Safonova, O.; Figi, R.; Weidenkaff, A.; Ferri, D. *J. Phys. Chem. C* **2010**, *114*, 4584–4594.
- (10) Koponen, M. J.; Suvanto, M.; Pakkanen, T. A.; Kallinen, K.; Kinnunen, T. J. J.; Harkonen, M. *Solid State Sci.* **2005**, *7*, 7–12.
- (11) Rodriguez, G. C. M.; Saruhan, B.; Petrova, O.; Gruenert, W. *Top. Catal.* **2009**, *52*, 1723–1727.
- (12) Ueda, A.; Yamada, Y.; Katsuki, M.; Kiyobayashi, T.; Xu, Q.; Kuriyama, N. *Catal. Commun.* **2009**, *11*, 34–37.
- (13) Tanaka, H.; Tan, I.; Uenishi, M.; Taniguchi, M.; Kimura, M.; Nishihata, Y.; Mizuki, J. *J. Alloys Compd.* **2006**, *408*, 1071–1077.
- (14) Tanaka, H.; Uenishi, M.; Taniguchi, M.; Tan, I.; Narita, K.; Kimura, M.; Kaneko, K.; Nishihata, Y.; Mizuki, J. *Catal. Today* **2006**, *117*, 321–328.
- (15) Tanaka, H.; Taniguchi, M.; Uenishi, M.; Kajita, N.; Tan, I.; Nishihata, Y.; Mizuki, J.; Narita, K.; Kimura, M.; Kaneko, K. *Angew. Chem., Int. Ed.* **2006**, *45*, 5998–6002.
- (16) Taniguchi, M.; Tanaka, H.; Uenishi, M.; Tan, I.; Nishihata, Y.; Mizuki, J.; Suzuki, H.; Narita, K.; Hirai, A.; Kimura, M. *Top. Catal.* **2007**, *42–43*, 367–371.
- (17) Li, J.; Singh, U. G.; Bennett, J. W.; Page, K.; Weaver, J. C.; Zhang, J.-P.; Proffen, T.; Rappe, A. M.; Scott, S. L.; Seshadri, R. *Chem. Mater.* **2007**, *19*, 1418–1426.
- (18) Li, J.; Singh, U. G.; Schladt, T. D.; Stalick, J. K.; Scott, S. L.; Seshadri, R. *Chem. Mater.* **2008**, *20*, 6567–6576.
- (19) Hegde, M. S.; Madras, G.; Patil, K. C. *Acc. Chem. Res.* **2009**, *42*, 704–712.
- (20) Bera, P.; Patil, K.; Jayaram, V.; Subbanna, G.; Hegde, M. *J. Catal.* **2000**, *196*, 293–301.
- (21) Prilokar, K. R.; Bera, P.; Sardoe, P. R.; Hegde, M. S.; Emura, S.; Kumashiro, R.; Lalla, N. P. *Chem. Mater.* **2002**, *14*, 2120–2128.
- (22) Baidya, T.; Priolkar, K. R.; Sarode, P. R.; Hegde, M. S.; Asakura, K.; Tateno, G.; Koike, Y. *J. Chem. Phys.* **2008**, *128*, 124711:1–8.
- (23) Baidya, T.; Dutta, G.; Hegde, M. S.; Waghmare, U. V. *Dalton Trans.* **2009**, 455–464.
- (24) Gupta, A.; Kumar, A.; Waghmare, U. V.; Hegde, M. S. *Chem. Mater.* **2009**, *21*, 4880–4891.
- (25) Baidya, T.; Gupta, A.; Deshpandey, P. A.; Madras, G.; Hegde, M. S. *J. Phys. Chem. C* **2009**, *113*, 4059–4068.
- (26) Gupta, A.; Hegde, M. S.; Priolkar, K. R.; Waghmare, U. V.; Sarode, P. R.; Emura, S. *Chem. Mater.* **2009**, *21*, 5836–5847.
- (27) Kurzman, J. A.; Ouyang, X.; Im, W. B.; Li, J.; Hu, J.; Scott, S. L.; Seshadri, R. *Inorg. Chem.* **2010**, *49*, 4670–4680.
- (28) Bueno-Lopez, A.; Krishna, K.; Makkee, M.; Moulijn, J. *Catal. Lett.* **2005**, *99*, 203–205.
- (29) Fornasiero, P.; Dimonte, R.; Rao, G. R.; Kaspar, J.; Meriani, S.; Trovarelli, A.; Graziani, M. *J. Catal.* **1995**, *151*, 168–177.
- (30) Hori, C. E.; Permana, H.; Ng, K. Y. S.; Brenner, A.; More, K.; Rahmoeller, K. M.; Belton, D. *Appl. Catal., B* **1998**, *16*, 105–117.
- (31) Kaspar, J.; Fornasiero, P.; Graziani, M. *Catal. Today* **1999**, *50*, 285–298.
- (32) Machida, M.; Murata, Y.; Kishikawa, K.; Zhang, D.; Ikeue, K. *Chem. Mater.* **2008**, *20*, 4489–4494.
- (33) Miki, T.; Ogawa, T.; Haneda, M.; Kakuta, N.; Ueno, A.; Tateishi, S.; Matsuura, S.; Sato, M. *J. Phys. Chem.* **1990**, *94*, 6464–6467.
- (34) Stark, W. J.; Maciejewski, M.; Madler, L.; Pratsinis, S. E.; Baiker, A. *J. Catal.* **2003**, *220*, 35–43.
- (35) Trovarelli, A. *Catal. Rev.* **1996**, *38*, 439–520.
- (36) Feng, M.; Goodenough, J. B. *Eur. J. Solid State Inorg. Chem.* **1994**, *31*, 663–672.
- (37) Ishihara, T.; Matsuda, H.; Takita, Y. *J. Am. Chem. Soc.* **1994**, *116*, 3801–3803.
- (38) Chan, K. S.; Ma, J.; Jaenicke, S.; Chuah, G. K.; Lee, J. Y. *Appl. Catal., A* **1994**, *107*, 201–227.
- (39) Dai, H. X.; He, H.; Li, W.; Gao, Z. Z.; Au, C. T. *Catal. Lett.* **2001**, *73*, 149–156.
- (40) Dai, H. X.; He, H.; Li, P. H.; Gao, L. Z.; Au, C. T. *Catal. Today* **2004**, *90*, 231–244.
- (41) Ouyang, X.; Scott, S. L. *J. Catal.* **2010**, *273*, 83–91.
- (42) Yamaguchi, O.; Takemura, H.; Yamashita, M.; Hayashida, A. *J. Electrochem. Soc.* **1991**, *138*, 1492–1494.
- (43) Brinks, H. W.; Fjellvag, H.; Kjekshus, A. *J. Solid State Chem.* **1997**, *129*, 334–340.
- (44) Shannon, R. D.; Prewitt, C. T. *Acta Crystallogr., Sect. B* **1969**, *25*, 925–946.
- (45) Shannon, R. D. *Acta Crystallogr., Sect. A* **1976**, *32*, 751–767.
- (46) Huang, Z. J.; Cao, Y.; Sun, Y. Y.; Xue, Y. Y.; Chu, C. W. *Phys. Rev. B* **1997**, *56*, 2623–2626.
- (47) Van Aken, B. B.; Palstra, T. T. M.; Filippetti, A.; Spaldin, N. A. *Nat. Mater.* **2004**, *3*, 164–170.
- (48) Smith, A. E.; Mizoguchi, H.; Delaney, K.; Spaldin, N. A.; Sleight, A. W.; Subramanian, M. A. *J. Am. Chem. Soc.* **2009**, *131*, 17084–17086.
- (49) Mizoguchi, H.; Sleight, A. W.; Subramanian, M. A. *Inorg. Chem.* **2011**, *50*, 10–12.
- (50) Béar, J.-F.; Garnier, P. *NIST Spec. Publ.* **1992**, 846, 212.
- (51) Hormillosa, C.; Healy, S.; Stephen, T.; Brown, I. D. Bond Valence Calculator, 1993 (<http://www.ccp14.ac.uk/ccp/web-mirrors/idbrown/>).
- (52) Scofield, J. H. *J. Electron Spectrosc. Relat. Phenom.* **1976**, *8*, 129.
- (53) Newville, M. *J. Synchrotron Radiat.* **2001**, *8*, 322–324.
- (54) Ravel, B.; Newville, M. *J. Synchrotron Radiat.* **2005**, *12*, 537–541.
- (55) Waser, J.; Levy, H. A.; Peterson, S. W. *Acta Crystallogr.* **1953**, *6*, 661–663.
- (56) Hultgren, R.; Zapffe, C. A. *Z. Kristallogr.* **1938**, *99*, 509–512.
- (57) Brunauer, S.; Emmett, P. H.; Teller, E. *J. Am. Chem. Soc.* **1938**, *60*, 309.
- (58) Barrett, E. P.; Joyner, L. G.; Halenda, P. P. *J. Am. Chem. Soc.* **1951**, *73*, 373–380.
- (59) Grosvenor, A. P.; Kobe, B. A.; Biesinger, M. C.; McIntyre, N. S. *Surf. Interface Anal.* **2004**, *36*, 1564–1574.
- (60) Gupta, R. P.; Sen, S. K. *Phys. Rev. B* **1975**, *12*, 15–19.
- (61) Kowalczyk, S. P.; Ley, L.; McFeely, F. R.; Shirley, D. A. *Phys. Rev. B* **1975**, *11*, 1721–1727.
- (62) McIntyre, N. S.; Zetaruk, D. G. *Anal. Chem.* **1977**, *49*, 1521–1529.
- (63) Fujimori, A.; Saeki, M.; Kimizuka, N.; Taniguchi, M.; Suga, S. *Phys. Rev. B* **1986**, *34*, 7318–7333.
- (64) Nesbitt, H. W.; Banerjee, D. *Am. Mineral.* **1998**, *83*, 305–315.
- (65) Oku, M.; Hirokawa, K.; Ikeda, S. *J. Electron Spectrosc. Relat. Phenom.* **1975**, *7*, 465–473.
- (66) Wagner, C. D.; Riggs, W. M.; Davis, L. E.; Moulder, J. F.; Muilenberg, G. E. *Handbook of X-ray Photoelectron Spectroscopy*; Physical Electronics Division, Perkin-Elmer Corp.: Eden Prairie, MN, 1979.

- (67) Kim, S.-J.; Lemaux, S.; Demazeau, G.; Kim, J.-Y.; Choy, J.-H. *J. Mater. Chem.* **2002**, *12*, 995–1000.
- (68) Garten, R. L.; Ollis, D. F. *J. Catal.* **1974**, *35*, 232–246.
- (69) Minai, Y.; Fukushima, T.; Ogasawara, S.; Ichikawa, M.; Tominaga, T. *J. Radioanal. Nucl. Chem.* **1986**, *106*, 167–173.
- (70) Niemantsverdriet, J. W.; Vankaam, J. A. C.; Flipse, C. F. J.; Vanderkraan, A. M. *J. Catal.* **1985**, *96*, 58–71.
- (71) Brayner, R.; Fillain, F.; Gengembre, L.; Ammar, S.; Bozon-Verduraz, F. *Eur. J. Inorg. Chem.* **2008**, *2008*, 1623–1631.
- (72) Samal, S. L.; Green, W.; Lofland, S. E.; Ramanujachary, K. V.; Das, D.; Ganguli, A. K. *J. Solid State Chem.* **2008**, *181*, 61–66.
- (73) Scanlon, D. O.; Morgan, B. J.; Watson, G. W. *Phys. Chem. Chem. Phys.* **2011**, *13*, 4279–4284.
- (74) Chiarello, G. L.; Ferri, D.; Grunwaldt, J.-D.; Forni, L.; Baiker, A. *J. Catal.* **2007**, *252*, 137–147.
- (75) Santhosh, K. M.; Eyssler, A.; Hug, P.; van Vegten, N.; Baiker, A.; Weidenkaff, A.; Ferri, D. *Appl. Catal., B* **2010**, *94*, 77–84.
- (76) Wei, X.; Hug, P.; Figi, R.; Trottmann, M.; Weidenkaff, A.; Ferri, D. *Appl. Catal., B* **2010**, *94*, 27–37.
- (77) Uenishi, M.; Tanaka, H.; Taniguchi, M.; Tan, I.; Nishihata, Y.; Mizuki, J.; Kobayashi, T. *Catal. Commun.* **2008**, *9*, 311–314.
- (78) Matsumura, D.; Nishihata, Y.; Mizuki, J.; Taniguchi, M.; Uenishi, M.; Tanaka, H. *J. Appl. Phys.* **2010**, *107*, 124319.
- (79) Luo, M. F.; Zheng, X. M. *Appl. Catal., A* **1999**, *189*, 15–21.
- (80) Singh, U. G.; Li, J.; Bennett, J. W.; Rappe, A. M.; Seshadri, R.; Scott, S. L. *J. Catal.* **2007**, *249*, 349–358.
- (81) Kato, S.; Ogasawara, M.; Sugai, M.; Nakata, S. *Solid State Ionics* **2002**, *149*, 53–57.
- (82) Tsipis, E. V.; Naumovich, E. N.; Shaula, A. L.; Patrakeev, M. V.; Waerenborgh, J. C.; Kharton, V. V. *Solid State Ionics* **2008**, *179*, 57–60.

NOTE ADDED AFTER ASAP PUBLICATION

This paper was published on the Web on July 29, 2011 with a minor error in the Title and Table 2. The corrected version was reposted on August 2, 2011.